Journal of Controlled Release 174 (2014) 37–42

Contents lists available at ScienceDirect

Journal of Controlled Release

journal homepage: www.elsevier.com/locate/jconrel

Evaluation of drug delivery to intact and porated skin by coherent Raman scattering and fluorescence microscopies

Natalie A. Belsey [a], Natalie L. Garrett [b], L. Rodrigo Contreras-Rojas [a], Adam J. Pickup-Gerlaugh [b], Gareth J. Price [c], Julian Moger [b], Richard H. Guy [a,*]

[a] Department of Pharmacy & Pharmacology, University of Bath, Bath, BA2 7AY, UK
[b] Department of Physics, University of Exeter, Exeter, EX4 4QL, UK
[c] Department of Chemistry, University of Bath, Bath, BA2 7AY, UK

ARTICLE INFO

Article history:
Received 25 July 2013
Accepted 4 November 2013
Available online 11 November 2013

Keywords:
Topical drug delivery
Stimulated Raman scattering (SRS)
Coherent anti-Stokes Raman scattering (CARS)
Confocal microscopy
Thermal poration of skin

ABSTRACT

Stimulated Raman scattering microscopy was used to assess the permeation of topically applied drugs and formulation excipients into porcine skin. This chemically selective technique generates high-resolution 3D images, from which semi-quantitative information may be elucidated. Ibuprofen, applied as a close-to-saturated solution in propylene glycol, was directly observed to crystallise in/on the skin, as the co-solvent permeated more rapidly, resulting in precipitation of the drug. Coherent Raman scattering microscopy is also an excellent tool, in conjunction with more conventional confocal fluorescence microscopy, with which to image micro/nanoparticle-based formulations. Specifically, the uptake of particles into thermal ablation transport pathways in the skin has been examined.

1. Introduction

The skin is an effective barrier, which has evolved to prevent entry of undesirable foreign substances into the body. However, despite the associated difficulties, topical drug delivery remains an attractive therapeutic approach (especially for the treatment of dermatological diseases) since it avoids the need for systemic exposure and its related disadvantages. To deliver drugs both safely and effectively through the skin, it is necessary to quantify the penetration of the active agent and to understand the 'metamorphosis' of the vehicle upon application and the disposition of key components of the vehicle. Currently, a widely-used approach involves removal of the stratum corneum (SC) by sequential adhesive tape stripping at specific time points, post-application of a formulation [1]. This enables generation of concentration profiles of the active and certain formulation ingredients; however, this method is both invasive and labour-intensive. In addition, it does not reveal information such as the pathway taken by the drug or the reasons for the poor penetration that is typically observed.

Coherent Raman scattering (CRS) microscopy provides a new tool with which to tackle this problem. CRS is a label-free imaging technique that is capable of real-time, non-invasive examination of living cells and organisms based on molecular vibrational spectroscopy. A coherent non-linear Raman signal is generated by focussing two synchronised ultrafast pulse trains into a sample with a difference in frequency matched to a Raman active mode of a molecular species of interest. The non-linear nature of this process confines the signal to a sub-micron focus that can be scanned in space, allowing three-dimensional mapping of bio-molecules in tissue with sub-cellular resolution.

CRS microscopy may be achieved by detecting either coherent anti-Stokes Raman scattering (CARS) [2,3] or stimulated Raman scattering (SRS) [4–10]. In CARS, the coherent anti-Stokes signal generated at frequency $\omega_{as} = 2\omega_p - \omega_S$, is spectrally isolated from the pump and Stokes beams using filters, and a signal intensity map can be obtained by raster scanning the pump and Stokes beams across the sample, allowing visualisation of the location of biomolecules of interest. The chemical specificity, strong signal strength and non-invasive imaging capabilities offered by CARS have been exploited in a wide range of biological studies, providing diverse information such as: the spectroscopic properties of diseased and healthy skin samples [3] and the interaction and uptake of nanoparticles within organs such as the liver [11] and the brain [12], as well as in living cells [13]. In contrast to CARS, SRS relies on detecting subtle changes in the intensities of the excitation fields that occur by virtue of stimulated excitation. When the difference frequency, $\omega_p - \omega_S$, matches a molecular vibrational frequency, the intensity of the Stokes beam, I_S, experiences a gain (SRG), ΔI_S, while the intensity of the pump beam, I_p, experiences a loss (SRL), ΔI_p. The intensity transfer from the pump to the Stokes beam only occurs when both beams are incident upon the sample and can be detected with high sensitivity using modulation transfer detection. Modulating the intensity of the Stokes beam modulates the SRS process and hence transfers an intensity modulation onto the pump beam. The amplitude of the transferred intensity modulation is directly proportional to the concentration of target molecules and by modulating at frequencies above laser noise

* Corresponding author.
E-mail address: r.h.guy@bath.ac.uk (R.H. Guy).

0168-3659/$ – see front matter © 2013 Elsevier B.V. All rights reserved.
http://dx.doi.org/10.1016/j.jconrel.2013.11.002

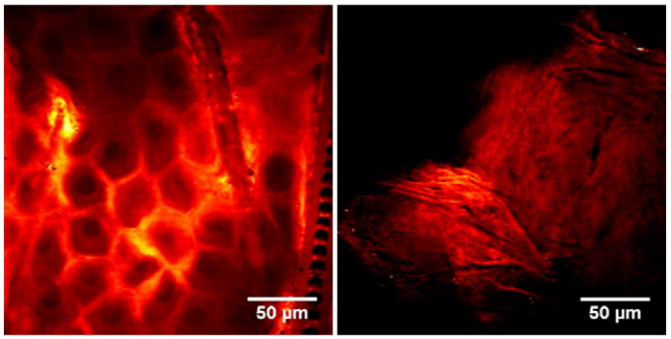

Fig. 1. SRS images obtained at 2855 cm^{-1} for CH_2 contrast. Left: mouse ear SC. Right: Porcine SC.

(>1 MHz) can be detected with a lock-in amplifier with great sensitivity (1 in 10^6).

For quantitative studies, SRS is often the more appropriate technique because the signal output is identical to the spontaneous Raman spectrum, and its linear concentration dependence affords a relatively straightforward quantitative analysis. These properties have proven to be efficacious in studies investigating drug interactions with skin both *in vitro* and *in vivo* [6,7]. CARS generates more complex vibrational spectra with a quadratic concentration dependence, making image interpretation much more challenging. However, for less quantitative studies, such as imaging particle-skin topology, CARS can be an excellent tool, since the high concentrations of chemical species present in particles generate strong signals due to the quadratic concentration dependence.

In the first part of this study, we demonstrate the differences in appearance between mouse and pig SC, the latter representing (as is widely accepted) a more appropriate model for the human barrier. Subsequently, ketoprofen is applied to porcine skin as a solution in perdeuterated propylene glycol. The architecture of the skin is imaged based on the contrast of the CH_2 groups present most notably in the skin lipids. The disposition of ketoprofen is visualised using the aromatic C – C contrast, and the propylene glycol-d_8 by the C – D bond. The data are compared to previous experiments on mouse ear skin [6].

We also demonstrate the suitability of these imaging techniques for characterising the effects of a device designed to aid the (trans)dermal delivery of compounds which permeate the skin particularly poorly; for example, macromolecules or very water-soluble and/or highly charged compounds. Thermal ablation generates small pores or channels within the SC by application of a short burst of heat, in this case, provided by a microarray of metal filaments. This serves to increase the permeability of the outer layer of the skin's barrier, without damaging the deeper layers of tissue. Here, we investigate the suitability of CRS microscopy, in combination with confocal fluorescence microscopy, for characterising the new transport pathways created by such a device, and the disposition of topically applied micro- and nano-particles within them.

2. Materials and methods

Porcine abdominal skin was cleaned with water, trimmed to remove excess hair and dermatomed to a nominal thickness of 300 μm. In an initial set of experiments, the skin was dosed with a solution of ketoprofen (Sigma-Aldrich, Gillingham, UK) in per-deuterated propylene glycol (Isotec, Ohio, USA), mounted for imaging as described below and then examined by SRS/CARS; the concentration of the drug in propylene glycol was 180 mg/mL. A short parallel study was also conducted in the same way during which the skin was treated with a solution of deuterated ibuprofen (Sigma-Aldrich, Gillingham, UK) in undeuterated propylene glycol (Sigma-Aldrich, Gillingham, UK) at a concentration of 380 mg/mL, corresponding to approximately 90% saturation [14]. For the ablation experiments, skin was treated with a poration device (PassPort™ A5A Applicator, Altea Therapeutics, Atlanta, GA, USA) immediately prior to mounting in a vertical Franz diffusion cell (Permegear, Hellertown, PA, USA), exposing a diffusion area of 2 cm^2. The receptor chamber was filled with phosphate-buffered saline solution (7.5 mL, pH 7.4). Particle suspensions (500 μL) were applied to the skin surface exposed in the donor chamber, which was subsequently covered with Parafilm® to prevent evaporation. The sample was incubated at 37 °C for a chosen duration, after which the Franz cell was dismantled, the particle suspension removed, and the skin immediately mounted for imaging.

Yellow–green fluorescent 0.02 μm and 2 μm diameter carboxylate-modified FluoSpheres® were purchased from Invitrogen (Eugene, OR, USA). Nanoparticles were prepared by free radical polymerization under a nitrogen atmosphere for 3 h from: ultrapure water (50 mL), sodium dodecyl sulphate (0.25 g, Sigma-Aldrich, Gillingham, UK) and methyl methacrylate (3.25 g, Sigma-Aldrich, Gillingham, UK). The resulting mixture was heated to 75 °C, and the reaction was initiated with potassium persulphate (25 mg, Sigma-Aldrich, Gillingham, UK). For deuterated particles, methyl methacrylate-d_8 (Sigma-Aldrich, Gillingham, UK) was substituted, and for the fluorescently labelled particles, fluorescein O-methacrylate (32.5 mg, Sigma-Aldrich, Gillingham, UK) was mixed with the methyl methacrylate before addition. The average particle diameter of 40 nm (with a polydispersity index of 0.1) was determined using dynamic light scattering (Zetasizer Nano S, Malvern Instruments Ltd, Worcestershire, UK).

All samples were mounted for imaging between two glass coverslips (22 × 50 mm^2 cover glasses Menzel-Gläser, Braunschweig, Germany). The slides were sealed together to reduce the loss of volatile substances and to minimise swelling/dehydration of tissue; the latter is of particular importance for lengthy time-course experiments. This was achieved using rectangular frames constructed from Parafilm. The frames were placed onto glass coverslips and the back of the slide was warmed on a heated stirrer-plate at 60 °C for a few seconds until the Parafilm became translucent. After cooling, the sample was placed within the confines of the frame, and a top coverslip applied. This glass slide was then sealed to the second one using a soldering iron, to melt the Parafilm, which then fused the two slides together. Utmost care was taken to contact the heat source only around the outer edges of the frame to prevent heat from reaching the sample. The glass slides were then secured inside a brass flow cell clamp for imaging. This served to prevent flexing

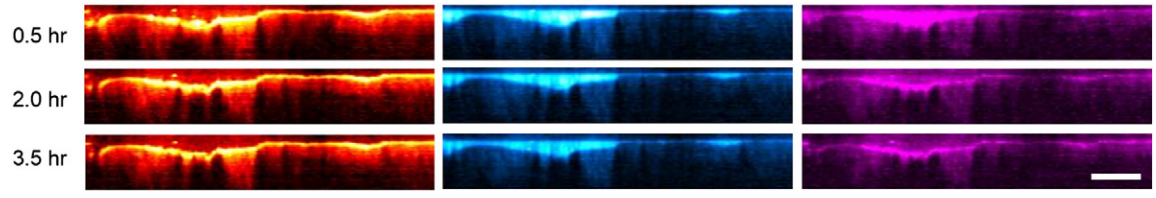

Fig. 2. SRS X–Z orthogonal view images of porcine skin dosed with ketoprofen in propylene glycol-d_8. Red/orange: 2855 cm^{-1} CH_2 stretching frequency. Cyan: PG-d_8 visualised at 2120 cm^{-1} (CD_2 stretch). Magenta: ketoprofen aromatic ring C – C stretch at 1599 cm^{-1}. Scale bar represents 100 μm.

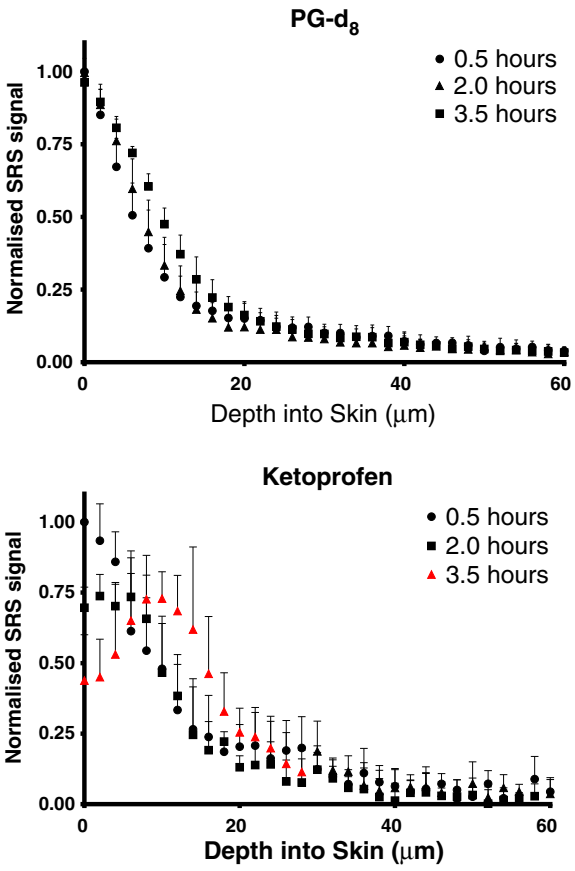

Fig. 3. Normalised SRS signal intensity as a function of depth into the skin. Average pixel intensity was determined using the 'plot z-axis profile' function in ImageJ. Error bars (above) depict standard deviation (n = 5). Red data points highlight the onset of ketoprofen crystallisation from the layer of formulation, onto the surface and within crevasses of the skin.

of the thin, pliable glass coverslips during the study. Laser power was minimised throughout to prevent damage to the biological samples examined.

CRS and two photon fluorescence (TPF) imaging were carried out using a custom-built multi-modal microscope comprising of a modified inverted microscope and confocal laser scanner (IX71 and FV300, Olympus UK). To optimise the transmission of the near IR light needed for CARS and SRS imaging, the standard galvanometer scanning mirrors were replaced with silver galvanometric mirrors and the tube lens was replaced by a MgF_2 coated lens. The dichroic mirror within the scan unit was replaced by a silver mirror, which gave high reflectivity throughout the visible and NIR (21010 Chroma Technologies). The light was focused onto the sample using either a 60× 1.2NA water immersion objective or a 20× 0.75NA air objective (UPlanS Apo, Olympus UK).

TPF was excited using a 800 nm output from a mode-locked femtosecond Ti:Sapphire laser (Mira 900 D, Coherent) with a pulse width of approximately 100 fs and a 76 MHz repetition rate. The signal was collected in the epi-direction using the objective lens and separated from the laser fundamental using a long pass dichroic mirror (670dcxr Chroma Technologies) and detected by a PMT (R3896, Hamamatsu) with filters (CG-BG-39 and F10-400-5-QBL, CVI laser) to isolate the TPF signal.

Synchronised, dual-wavelength picosecond excitation required for CRS was provided by an optical parametric oscillator (OPO) (Levante Emerald, APE-Berlin) synchronously pumped at 532 nm by a frequency doubled Nd:YVO4 laser (picoTRAIN, High-Q GmB), delivering 7 ps pulses at a repetition rate of 76 MHz. The pump-laser fundamental (1064 nm) was also available as a separate output. The OPO uses a temperature-tuned, non-critically phase matched LBO crystal to allow continuous tuning of the OPO signal from 690 to 980 nm by adjustment of the LBO temperature and an inter-cavity Lyot filter. The OPO signal and pump-laser fundamental were used as the pump and Stokes beams, respectively, for CARS and SRS, and as the probe and excitation beams for two photon photothermal lensing. The two pulse trains were spatially overlapped on a dichroic mirror (1064 DCRB, Chroma Technology) and temporally overlapped using a delay-stage. Before entering the microscope, the 1064 nm beam was amplitude modulated at 1.7 MHz using an acousto-optic modulator (Crystal Technologies Inc., type S/N 3080-197).

The CARS signal was detected in the epi-detection by the objective, spectrally isolated from the pump and Stokes beams using a dichroic mirror (750LP, Chroma) and band pass filter (750/210, Chroma) and detected using a red-sensitive PMT (R3896, Hamamatsu) mounted on the rear port of the microscope. SRS was detected in the forward direction by a 1.0NA condenser lens (LUMFI, Olympus) and a large area photodiode (FDS1010, Thorlabs). A bandpass filter (850/90 nm, Chroma) was mounted in front of the detector to block the modulated 1064 nm beam. A lock-in amplifier (SR844, Stanford Research Systems) was used to detect the SRS signal with a time constant of 30–100 μs. SRS images were generated by recording either the X or R outputs from the

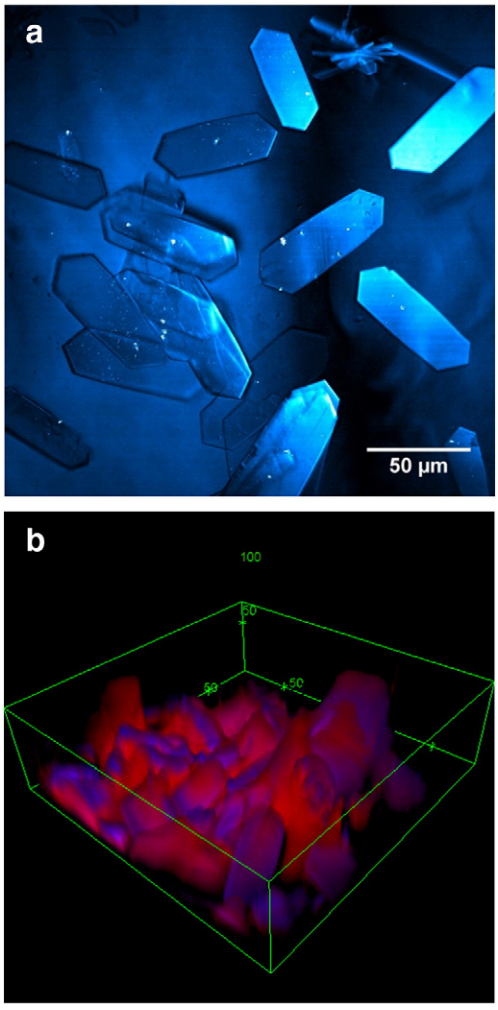

Fig. 4. Crystals of Ibuprofen-d_3 formed in/on the skin within 30 min post application. Panel (a): SRS contrast was obtained at 2120 cm^{-1} corresponding to C – D stretch. Panel (b) depicts a still from a video rotation of a 3D projection created by 'colour merge' of the C – D contrast (blue, for ibuprofen) with the corresponding CH_2 signal emanating from the skin lipids (red) to reveal the topology.

lock-in. Images were processed using ImageJ, a Java-based image processing program [15].

Laser scanning confocal microscopy images were obtained using a 510 Meta inverted confocal laser scanning microscope (Carl Zeiss, Jena, Germany). Samples were excited using a 405 nm (diode) and a 488 nm (argon) laser. EC Plan-Neofluar M27 objectives were used for image acquisition (40×/1.30 oil DIC, or 20×/0.50 air). Fluorescence signals were recorded as separate channels at 420–480 nm (blue), and 505–530 nm (green).

3. Results and discussion

3.1. Porcine vs. mouse ear skin

Images of un-dosed tissue were recorded for both porcine skin and mouse ear skin (Fig. 1). The mouse ear skin generated very clear images, in which the hexagonal shaped corneocytes are clearly visible, framed by the strong signal generated by the intercellular lipids. Porcine SC, however, showed considerably less structural detail. The pig skin used for this experiment had been specially prepared with a scalpel to ensure comparable thickness to mouse ear skin, yet individual corneocytes were still difficult to identify. While mouse SC typically has 3–5 columnar-stacked layers of corneocytes, porcine SC is composed of approximately 20 layers of these cells, which are less regularly arranged but more densely stacked [16]. It is possible, therefore, that this higher stacking density in pig skin gives rise to convoluted corneocyte layers within the experimental z-resolution (1 μm) of the technique, thereby obscuring the finer detail visible in mouse SC.

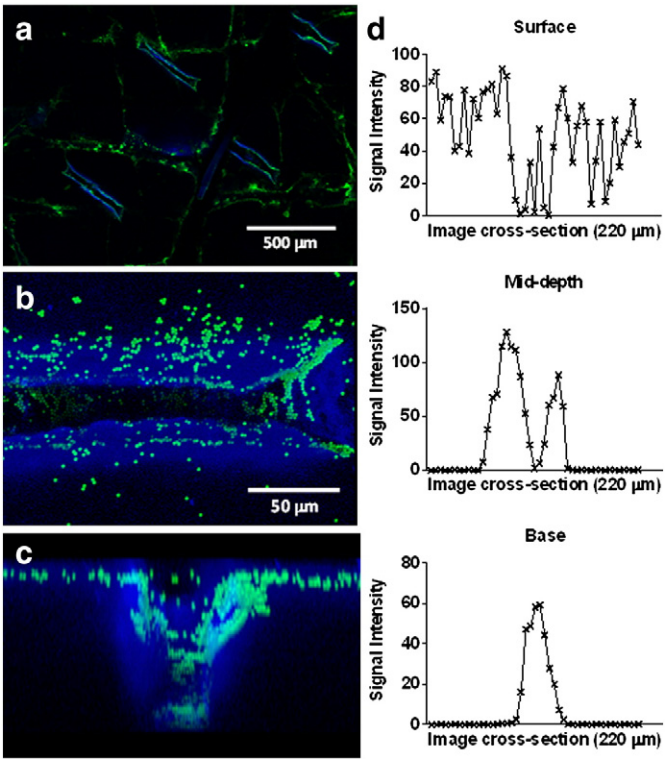

Fig. 5. Confocal microscopy images of 0.02 μm (panel a) and 2 μm (panels b and c) FluoSpheres® (green, 488 nm) on thermally ablated porcine skin (visualised via its autofluorescence (blue) at 405 nm). Panel (a): Tile view stitched images to reveal the patterned array of the 'trenches' created by the device. Panel (b): Projection from above of an individual 'trench'. Panel (c): Orthogonal view of the panel (b) image stack. Panel (d): Fluorescent signal intensity profiles transecting the channel at the surface, mid-depth, and base (average values plotted across 10 pixels).

In this study, SRS was recorded in the forward direction, so samples were chosen to be as thin as possible without compromising the integrity of the barrier. It was found that dermatoming to 300 μm was optimal. It should also be noted that mouse ear skin was taken from white mice because the pigmentation present in brown mouse skin absorbs much more strongly than its surroundings, causing localised burning, and making imaging much more challenging. The porcine skin used was therefore screened carefully to avoid pigmentation spots.

Although the mouse ear skin displayed more prominent features, its barrier function is recognised as inferior to that of the human counterpart. Porcine skin, which was used here, on the other hand, is widely accepted as an excellent model for the human tissue [17].

3.2. Drug permeation time course experiment

A time course experiment on porcine skin dosed with ketoprofen in deuterated propylene glycol was performed by sequentially tuning the lasers between 2855 cm^{-1} to image the skin lipids, to 2120 cm^{-1} to image C–D contrast of the propylene glycol, and then to 1599 cm^{-1} to obtain contrast for the aromatic C–C stretch of the ketoprofen. A fourth off-resonance wavelength (1554 cm^{-1}) was also recorded to verify that the signal vanished when the wavelength was tuned away from the resonance frequency.

It was subsequently possible to extract quantitative information from the series of images (XZ orthogonal views of the 3D image stack are displayed in Fig. 2). However, for superior analysis, a number of factors needed to be carefully addressed: fluctuations in laser intensity, sample movement/swelling, particles of dirt, background signal emanating from the skin itself, defining the surface of the skin (since it is not flat), and sufficient formulation coverage to assume an excess for the experimental duration.

The average pixel intensity of each of 5 delimited regions (20 by 20 pixels) was determined using 'specify' and then 'plot z-stack profile' plugins in ImageJ to generate profiles of SRS signal *versus* depth into the skin (Fig. 3). Regions for analysis were selected on the basis of their sufficiently thick coverage of formulation. SRS signal was normalised against the signal recorded at a secondary detector (using a beam splitter) to account for any fluctuations in laser intensity. The surface of the skin within each region was defined by taking the first derivative of the SRS signal at the CH_2 frequency, and designating the maxima as '0 μm' sample depth. It should be noted that the surface of the skin is quite uneven; therefore '0 μm' should be considered an approximation. Adjustments were made where necessary to correct for small movement shifts, detected by visual inspection of structural features captured in the images. The SRS signal (average pixel intensity) at the surface '0 μm' on the first time point was designated 1.00 and subsequent depths and time points were plotted as a fraction of this value. Small amounts of background signal (*e.g.*, from particles of dirt), detected at the off-resonance wavelength were separated from the SRS resonant signal before normalisation. Regions containing very bright spots caused by dirt were avoided since their strong signal would have clearly affected the numerical results.

Fig. 3 shows the semi-quantitative data extracted from a series of images recorded over 3.5 h. The profiles show similar features to those obtained for ibuprofen using the tape stripping approach and human skin [14,18]. Notably, permeation occurred more slowly than determined previously by SRS for mouse skin [6], as would be expected. A visual inspection of the orthogonal images of the ketoprofen signal reveals that, over the duration of the experiment, the drug began to crystallise out and form a solid layer on the surface of the skin. Close inspection shows a uniform intensity band of ketoprofen on the surface of the skin after 30 min; however, by 3.5 h post-application, there is a bright, narrow band hugging the topology of the skin, while the drug concentration in the upper region of the formulation had dropped. This feature manifests itself in the profile of the SRS signal in Fig. 3: the data at the earlier time-points show the expected monotonic

decay from the maximum measured at the surface of the skin (*i.e.*, in parallel with the propylene glycol signal). In contrast, by 3.5 h the ketoprofen profile looks very different in this region (data points shown in red for clarity). At 0 μm, the 3.5 hour profile signal has fallen to just under 50% of its original value, and instead begins to rise towards the superficial layers of the skin, where the drug has formed a layer of solid on the surface and within accessible crevices. The inhomogeneity of the crystalline deposits on the surface at this time point generates larger standard deviation between sites.

It should be noted that SRS signal is attenuated with increasing depth into the sample. The data presented have not been corrected for this signal loss, and thus data presented here are of a semi-quantitative nature. An important future step in the development of this technique will involve modelling this signal drop in order to perform a reliable correction to account for the loss. However, this is non-trivial since it will be heavily sample-dependent and will be affected by a variety of factors such as density and refractive index of topical formulations (changing with permeation) in addition to differences between skin samples.

An even more extreme example of this phenomenon was observed with ibuprofen, as had been previously reported using mouse skin [6]. Following application of a propylene glycol solution of deuterated ibuprofen-d_3 to the skin at a concentration close to its saturation solubility, large, geometric crystals were clearly visible, having formed within 30 min post-application of the formulation (Fig. 4). Video data showing progressive depth into the skin, in addition to rotating 3D images, which depict the topology of the crystals on the skin are presented in Supplementary information A and B respectively (available on-line).

3.3. Particle uptake into thermal ablation channels

Confocal fluorescence microscopy was first used to image yellow–green fluorescent, 2 μm diameter microparticles (FluoSpheres®) on skin, which had been pre-treated with a thermal ablation device. In the images presented below, the green signal at 488 nm corresponds to the fluorescein label on the FluoSpheres®, while the blue emission at 405 nm reflects skin autofluorescence.

In panel (a) of Fig. 5, the confocal microscopy image shown was obtained using a 'tile' function, to stitch together a 5 × 5 field-of-view grid to enable visualisation of the array of rectangular, trench-like structures created by the device. Panel (b) focuses on a single 'trench' created by the porator, and individual particles are clearly visualised. Panel (c) displays the corresponding orthogonal view of this image stack. Skin autofluorescence is heightened around the trench boundaries, which may be caused by tissue compaction, or localised burning post-ablation. Panel (d) plots the variation in fluorescence across the orthogonal image at the surface, mid-depth and base of the channel, corresponding to the fluorescent particles adhering to the topology of the structure.

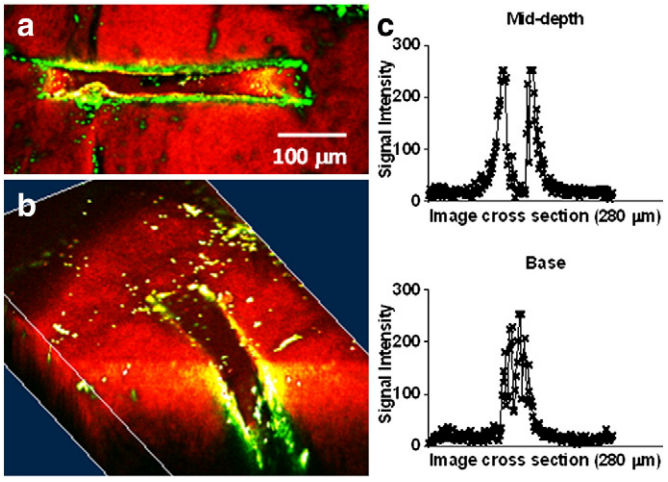

Fig. 6. Porated skin incubated for 1 h with 2 μm diameter FluoSpheres®. CARS contrast (CH_2 stretching) was recorded at 2855 cm^{-1} (red). TPF was recorded at 813 nm (green). Images were recorded at 1 μm depth increments. Panel (a): XY view of a channel. Panel (b): 3D cross-section of the channel (prepared using the ImageJ 'volume viewer' plugin). Panel (c): Fluorescence signal intensity profiles transecting the channel at the mid-depth and base.

The images confirm that the channels created by the device are approximately 300 μm long, 50 μm wide, and up to 100 μm deep (z-direction). The 3D images obtained reveal the clustering of particles on the surface of the skin, within natural creases, and within the channels created by the device. No evidence was observed for the permeation of FluoSpheres® outside the boundaries of the pores.

In addition to confocal microscopy, the experiment was also performed using a combination of TPF and CARS to reveal further detail of the 3D architecture of the skin (Fig. 6). Panel (a) of Fig. 6 illustrates a thermally porated 'trench' in the skin, where the red CARS signal from endogenous lipids is absent and replaced only by a dark rectangle. This surface image reveals the presence of the green–yellow microparticles in the 'crevasses' of the skin and at the edges of the trench, in a manner consistent with that observed in Fig. 5. An animated scan of this image stack is available by accessing Supplementary Video C (available on-line). Panel (b) of Fig. 6 shows a 3D reconstruction of a 'trench' with microparticles visible along the walls and at the base of the pore created by the device. The fluorescence signal intensity profiles in panel (c) provide a semi-quantitative confirmation of this visual observation. At the mid-depth of the 'trench', a substantial signal from particles that adhered to the walls is detected while there is no detectable fluorescence from the (presumably empty) centre of the pore. In contrast, at the base of the trench, as might be expected, there is accumulation of particles and a large fluorescent signal.

Although fluorescence-based imaging techniques are suitable when studying large particles, which can be individually visualised, smaller-sized particles present a greater challenge for accurate analysis. The subsequent experiments, performed using nanoparticles of 40 nm diameter that were prepared from a methyl methacrylate monomer, incorporating a small amount of fluorescein to enable visualisation using TPF, illustrate this point.

Panels (a–c) of Fig. 7 show fluorescently labelled nanoparticles on the skin surrounding an ablation pore. Since the skin itself produces auto-fluorescence, it is difficult to determine whether the low-level signal is originating from a small amount of particles or from the skin itself, because the particles are too small to be individually distinguished. For example, panel (b) shows a confocal slice mid-depth through the trench; while it was expected (and it is most probably the case) that the nanoparticles would be confined to the pore, there is a confounding green haze to the surrounding tissue. The cross-section in panel (c), while apparently confirming the anticipated distribution of particles to the walls and base of the 'trench', does not entirely remove this potential ambiguity.

Consequently, a second batch of nanoparticles was prepared; this time using deuterated methyl methacrylate monomer (rather than fluorescein) to enable their visualisation on and within the skin by SRS. The resulting images (Fig. 7, panels (d–e)), due to the chemical specificity of the Raman CD_2 signal, are clear-cut. The blue signal originates exclusively from the deuterated methacrylate monomer incorporated into the nanoparticles confirming that they are exclusively confined to crevasses in the skin surface and to within the confines of the ablation pore. An animated scan of the panel (d) stack is available by accessing Supplementary Video D (available on-line).

4. Conclusions

While images of mouse ear skin obtained with SRS reveal greater structural detail than those from porcine skin of comparable thickness, the acquisition of Raman signal in the forward direction from thinner

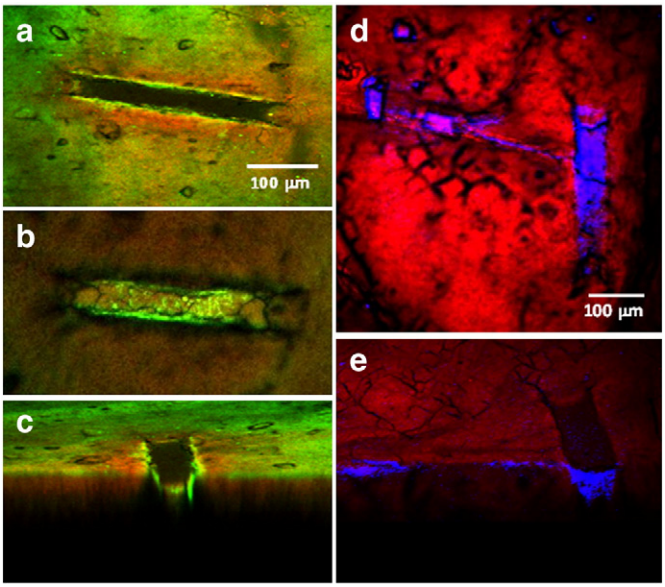

Fig. 7. Porated skin incubated for 12 h with 40 nm diameter particles. CARS contrast was recorded at 2855 cm^{-1} (CH2, red). Panels (a–c): Fluorescent methyl methacrylate particles; TPF was recorded at 815 nm (green); images were recorded at 0.5 μm depth increments. Panels (d–e): Deuterated methyl methacrylate particles; SRS (CD_2) at 2120 cm^{-1} (blue); images were recorded at 1 μm depth increments.

samples enabled good quality images to be captured. The uptake of formulation constituents by the skin can cause some swelling of the tissue, but any three-dimensional movement can be tracked by monitoring the CH_2 stretching signal from skin lipids; that is, because Raman scattering permits physiological structures in the skin to be visualised and used as 'landmarks' to decouple chemical diffusion across the skin from tissue movement.

Although deuteration of chemicals of interest is not an absolute requirement, it can provide significant benefit in the event that there is not a set of wavelengths at which contrast for the skin, drug and vehicle can be exclusively obtained. In addition, the CD_2 wavelength gives rise to extremely low levels of SRS signal from skin itself, and affords optimum contrast as a result.

Although SRS is presently unable to quantify *absolute* concentration gradients of drug or excipient across the skin as is possible using tape stripping and subsequent chemical analysis (*e.g.*, by HPLC), it offers valuable mechanistic information, such as the transport pathway taken by the penetrant, and the 'metamorphosis' of the formulation, including crystallisation of the drug; in other words, key visual insight which is not accessible using alternative techniques. In addition, SRS is an excellent tool with which to investigate the effects of skin ablation devices, and to determine the disposition of nanoparticles in such porated skin, in particular those too small to be individually visualised.

Acknowledgements

Financial support for this project was provided by GLAXOSMITHKLINE Research & Development, Ltd. (London, U.K.) and, in part, by LEO Pharma A/S (Ballerup, Denmark). L.R.C-R is the recipient of a doctoral fellowship from CONACyT, Mexico. The authors thank Altea Therapeutics for the provision of the PassPort™ poration device, and Dr Adrian Rogers (MAS suite, University of Bath) for the assistance with confocal imaging.

Supplementary data to this article can be found online at http://dx.doi.org/10.1016/j.jconrel.2013.11.002.

References

[1] C. Herkenne, I. Alberti, A. Naik, Y.N. Kalia, F.X. Mathy, V. Preat, R.H. Guy, *In vivo* methods for the assessment of topical drug bioavailability, Pharm. Res. 25 (2008) 87–103.
[2] C.L. Evans, E.O. Potma, M. Puoris'haag, D. Cote, C.P. Lin, X.S. Xie, Chemical imaging of tissue *in vivo* with video-rate coherent anti-Stokes Raman scattering microscopy, Proc. Natl. Acad. Sci. U. S. A. 102 (2005) 16807–16812.
[3] H.G. Breunig, R. Buckle, M. Kellner-Hofer, M. Weinigel, J. Lademann, W. Sterry, K. Konig, Combined *in vivo* multiphoton and CARS imaging of healthy and disease-affected human skin, Microsc. Res. Tech. 75 (2012) 492–498.
[4] C.W. Freudiger, W. Min, B.G. Saar, S. Lu, G.R. Holtom, C. He, J.C. Tsai, J.X. Kang, X.S. Xie, Label-free biomedical imaging with high sensitivity by stimulated Raman scattering microscopy, Science 322 (2008) 1857–1861.
[5] W. Min, C.W. Freudiger, S. Lu, C. He, J.X. Kang, X.S. Xie, Stimulated Raman scattering microscopy for biomedical imaging, in: A.S.P.T.C. Periasamy (Ed.), Multiphoton Microscopy in the Biomedical Sciences Ix, 2009.
[6] B.G. Saar, L.R. Contreras-Rojas, X.S. Xie, R.H. Guy, Imaging drug delivery to skin with stimulated Raman scattering microscopy, Mol. Pharm. 8 (2011) 969–975.
[7] B.G. Saar, C.W. Freudiger, J. Reichman, C.M. Stanley, G.R. Holtom, X.S. Xie, Video-rate molecular imaging *in vivo* with stimulated Raman scattering, Science 330 (2010) 1368–1370.
[8] W. Min, C.W. Freudiger, S. Lu, X.S. Xie, Coherent nonlinear optical imaging: Beyond fluorescence microscopy, in: S.R. Leone, P.S. Cremer, J.T. Groves, M.A. Johnson (Eds.), Annual Review of Physical Chemistry, Vol. 62, 2011, pp. 507–530.
[9] Y. Ozeki, F. Dake, S.i. Kajiyama, K. Fukui, K. Itoh, Analysis and experimental assessment of the sensitivity of stimulated Raman scattering microscopy, Opt. Express 17 (2009) 3651–3658.
[10] Y. Ozeki, W. Umemura, Y. Otsuka, S. Satoh, H. Hashimoto, K. Sumimura, N. Nishizawa, K. Fukui, K. Itoh, High-speed molecular spectral imaging of tissue with stimulated Raman scattering, Nat. Photonics 6 (2012) 844–850.
[11] N.L. Garrett, A. Lalatsa, D. Begley, L. Mihoreanu, I.F. Uchegbu, A.G. Schoetzlein, J. Moger, Label-free imaging of polymeric nanomedicines using coherent anti-Stokes Raman scattering microscopy, J. Raman Spectrosc. 43 (2012) 681–688.
[12] M. Mazza, R. Notman, J. Anwar, A. Rodger, M. Hicks, G. Parkinson, D. McCarthy, T. Daviter, J. Moger, N. Garrett, T. Mead, M. Briggs, A.G. Schatzlein, I.F. Uchegbu, Nanofiber-based delivery of therapeutic peptides to the brain, ACS Nano 7 (2013) 1016–1026.
[13] N. Garrett, M. Whiteman, J. Moger, Imaging the uptake of gold nanoshells in live cells using plasmon resonance enhanced four wave mixing microscopy, Opt. Express 19 (2011) 17563–17574.
[14] C. Herkenne, A. Naik, Y.N. Kalia, J. Hadgraft, R.H. Guy, Effect of propylene glycol on ibuprofen absorption into human skin *in vivo*, J. Pharm. Sci. 97 (2008) 185–197.
[15] W.S. Rasband, ImageJ, http://imagej.nih.gov/ij/ U.S. National Institutes of Health, Bethesda, Maryland, USA, 1997–2013.
[16] P. Wertz, D. Downing, Stratum corneum: biological and biochemical considerations, in: J. Hadgraft, R. Guy (Eds.), Transdermal Drug Delivery, Marcel Dekker, New York, 1989, pp. 1–22.
[17] N. Sekkat, R.H. Guy, Biological Models to Study Skin Permeation, Pharmacokinetic Optimization in Drug Research, 2001. 155–172.
[18] C. Herkenne, A. Naik, Y.N. Kalia, J. Hadgraft, R.H. Guy, Ibuprofen transport into and through skin from topical formulations: *in vitro–in vivo* comparison, J. Investig. Dermatol. 127 (2007) 135–142.